Engineering Mechanics Unit

Utilising Direct Simulation Monte Carlo Methods (DSMC) to Model Rarefied Gas Flow under Various Conditions

Pradyumnan R

Summer Research Fellowship Programme 2024

July 16, 2024

Bengaluru

To my parents and my brother, for understanding and supporting me from back home.

Acknowledgements

I would like to acknowledge and give my warmest thanks to **Prof. Meheboob Alam** who made this work possible. His guidance and insight have been invaluable. I would also like to thank **Dr. Manojit Ghosh** for his willingness to help and answer my questions at any time.

I would like to express my sincerest gratitude to the **Jawaharlal Nehru Centre for Advanced Scientific Research (JNCASR)** and the **Engineering Mechanics Unit** at JNCASR for providing me with the resources and environment that enabled me to work comfortably.

Abstract

Proposed by Graeme Bird in 1963, the Direct Simulation Monte Carlo (DSMC) method has been steadily gaining popularity in the scientific community, owing to both its robustness, rapidly improving computational power, and parallelization paradigms. This work starts by looking into some fundamental assumptions that continuum fluid mechanics is based on, explores the conditions under which these fail, and later explores some alternative techniques to model fluid flow. Additionally, a DSMC tool called SPARTA will be looked into, and existing studies showing its validity will be summarized. After this, the work moves on to discuss some simulations that have been set up, and their agreement with the predicted results will be scrutinized. Finally, some possible future directions for the work are discussed, detailing a research direction involving investigating fluid flow in Martian atmospheric conditions.

List of Figures

Contents

CHAPTER 1

Introduction

1.1 Continuum Mechanics

Continuum mechanics is a branch of mechanics that deals with the deformation of and transmission of forces through materials modeled as a continuous medium rather than as discrete particles. A continuum is a body that can be continually subdivided into infinitesimal elements with local material properties defined at any particular point. Properties of the bulk material can therefore be described by continuous functions, and their evolution can be studied using the mathematics of calculus. It can be broadly divided into **fluid mechanics** and **solid mechanics**.

1.2 Fluid Mechanics

Fluid mechanics is the branch of physics concerned with the mechanics of fluids (liquids, gases, and plasmas) and the forces on them. It can be divided into *fluid statics*, the study of fluids at rest; and *fluid dynamics*, the study of the effect of forces on fluid motion. Being a branch of *continuum mechanics*, it models matter from a macroscopic viewpoint.

Modeling fluids mathematically can be quite complex and is an active field of research. Many problems in fluid mechanics that haven't been solved analytically are often solved using numerical methods employing computers. *Computational Fluid Dynamics (CFD)* is a field devoted to

this approach.

A popular mathematical model for describing continuum fluid flow is the **Navier-Stokes equations**. It is a set of partial differential equations that describe the motion of viscous fluid substances. The most general form of the Navier-Stokes equation is given below,

$$\rho\left(\frac{\partial \boldsymbol{u}}{\partial t}+(\boldsymbol{u}\cdot\boldsymbol{\nabla})\,\boldsymbol{u}\right)=-\boldsymbol{\nabla}p+\boldsymbol{\nabla}\cdot\left\{\mu\left[\boldsymbol{\nabla}\boldsymbol{u}+(\boldsymbol{\nabla}\boldsymbol{u})^{T}-\frac{2}{3}(\boldsymbol{\nabla}\cdot\boldsymbol{u})\boldsymbol{I}\right]\right\}+\boldsymbol{\nabla}\left[\zeta\,(\boldsymbol{\nabla}\cdot\boldsymbol{u})\right]+\rho\boldsymbol{f} \quad (1.1)$$

where $\boldsymbol{u}$ is the velocity field, p is the pressure field, μ is the dynamic coefficient of viscosity, ζ is the bulk viscosity and $\boldsymbol{f}$ is the body force field per unit volume, all of the fluid under consideration.

Though this model is used widely to describe several phenomena observed, it fails when some of the underlying assumptions fail. The most fundamental assumption underlying the Navier-Stokes equations is the **continuum assumption**. When the continuum assumption fails, the solutions predicted by the Navier-Stokes equations start to deviate from the observed solutions. How close a flow is to satisfying the continuum assumption is given by the **Knudsen number** of the flow. The Knudsen number of a flow is described by the equation given below,

$$Kn=\frac{\lambda}{L^{*}} \quad (1.2)$$

where λ is the mean free path of the molecules comprising the fluid and L^{*} is the characteristic length scale of the problem.

As the Knudsen number approaches 0, the continuum assumption starts to yield solutions closer to the physical solutions. A few regimes for the knudsen number are given in Figure 1.1.

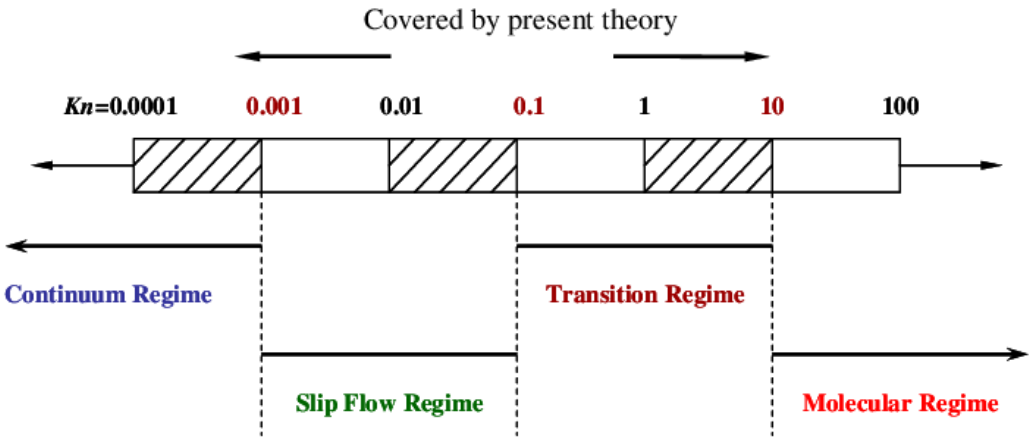

Fig. 1.1: Various regimes according to the knudsen number [Source : Google]

As a flow starts having knudsen numbers greater than 0.001, the Navier-Stokes equations start to deviate from the physical solutions in their original form. To obtain solutions in these ranges of the knudsen number, one can use other models such as *Smoothed Particles Hydrodynamics (SPH)* or *Burnett equations* to model flow mathematically. Another popular method involves applying Newton's laws of motion on particles individually referred to as *Molecular Dynamics (MD)*. MD is generally implemented numerically using computers. Apart from these methods, one can even solve the *Boltzmann equation* directly for the particles constituting the fluid. Solving the Boltzmann equation is a stochastic method as it considers a set of particles rather than individual particles. Both MD and Boltzmann equations offer a model that no longer considers a fluid to be a continuum, allowing them to capture a wide range of physical phenomena that conventional continuum models fail to capture.

The DSMC method was first proposed by Graeme Bird [1]. DSMC uses probabilistic Monte Carlo simulation to solve the Boltzmann equation for finite Knudsen number flows. Since the introduction of DSMC, it has been gradually gaining more attention. One of the most popular open-source codes available for DSMC called SPARTA was developed by Sandia National Laboratories under the US Department of Energy.

Both the Boltzmann equation and the DSMC method are discussed in more detail in chapters 2 and 3.

CHAPTER 2

Boltzmann Equation

The Boltzmann equation describes the statistical behaviour of a thermodynamic system not in a state of equilibrium. The equation is not the result of analysing every individual particle but is rather a result of considering a probability distribution of the position and momentum of a typical particle. In other words, it's the probability that a particle occupies a very small region of space centred around $\boldsymbol{r}$ (represented as $d^3\boldsymbol{r}$) and momentum nearly equal to $\boldsymbol{p}$ (represented as $d^3\boldsymbol{p}$) at an instant of time.

2.1 The Phase Space and the Density Function

The set of all positions $\boldsymbol{r}$ and momenta $\boldsymbol{p}$ parameterised by time t is called the *phase space* of the system. This space is 6-dimensional. If we define a probability distribution function $f(\boldsymbol{r},\boldsymbol{p},t)$, then we obtain the number of particles (dN) in $d^3\boldsymbol{r}d^3\boldsymbol{p}$ as,

$$dN = f(\boldsymbol{r},\boldsymbol{p},t)d^3\boldsymbol{r}d^3\boldsymbol{p} \tag{2.1}$$

Integrating over positions and momenta, we obtain,

$$N = \int_{momenta} d^3\boldsymbol{p} \int_{positions} d^3\boldsymbol{r} f(\boldsymbol{r},\boldsymbol{p},t) \tag{2.2}$$

2.2 Principal Statement

The general equation is given by,

$$\frac{df}{dt} = \left(\frac{\partial f}{\partial t}\right)_{force} + \left(\frac{\partial f}{\partial t}\right)_{diff} + \left(\frac{\partial f}{\partial t}\right)_{coll} \tag{2.3}$$

where the *force* term corresponds to the forces exerted on the particles by an external influence, *diff* refers to the diffusion of the particles and *coll* refers to the forces due to particle collisions.

2.2.1 Force and Diffusion Terms

Suppose there are particles with position $\boldsymbol{r}$ in $d^3\boldsymbol{r}$ and momentum $\boldsymbol{p}$ in $d^3\boldsymbol{p}$ at time t. If a force $\boldsymbol{F}$ acts instantaneously on all particles, then at $t+\Delta t$, we have $\boldsymbol{r}+\Delta\boldsymbol{r} = \boldsymbol{r}+\frac{\boldsymbol{p}}{m}\Delta t$ and $\boldsymbol{p}+\Delta\boldsymbol{p} = \boldsymbol{p}+\boldsymbol{F}\Delta t$. In the absence of collisions, if we write an equation for the number of particles, we obtain,

$$f(\boldsymbol{r}+\frac{\boldsymbol{p}}{m}\Delta t, \boldsymbol{p}+\boldsymbol{F}\Delta t, t+\Delta t)d^3\boldsymbol{r}d^3\boldsymbol{p} = f(\boldsymbol{r},\boldsymbol{p},t)d^3\boldsymbol{r}d^3\boldsymbol{p} \tag{2.4}$$

In the above equation, we have used the fact that the phase space volume element is constant. However, if there are collisions, the particle density in phase space volume changes, and as a result we obtain,

$$dN_{coll} = \left(\frac{\partial f}{\partial t}\right)_{coll} \Delta t d^3\boldsymbol{r}d^3\boldsymbol{p} \tag{2.5}$$

$$= \left(f(\boldsymbol{r}+\frac{\boldsymbol{p}}{m}\Delta t, \boldsymbol{p}+\boldsymbol{F}\Delta t, t+\Delta t)d^3\boldsymbol{r}d^3\boldsymbol{p} - f(\boldsymbol{r},\boldsymbol{p},t)\right) d^3\boldsymbol{r}d^3\boldsymbol{p} \tag{2.6}$$

$$= \Delta f d^3\boldsymbol{r}d^3\boldsymbol{p} \tag{2.7}$$

Dividing by the phase space volume and Δt and taking $\Delta f, \Delta t \to 0$, we obtain,

$$\frac{df}{dt} = \left(\frac{\partial f}{\partial t}\right)_{coll} \tag{2.8}$$

The total differential of f is,

$$df = \frac{\partial f}{\partial t}dt + \left(\frac{\partial f}{\partial x}dx + \frac{\partial f}{\partial y}dy + \frac{\partial f}{\partial z}dz\right) + \left(\frac{\partial f}{\partial p_x}dp_x + \frac{\partial f}{\partial p_y}dp_y + \frac{\partial f}{\partial p_z}dp_z\right) \tag{2.9}$$

$$= \frac{\partial f}{\partial t}dt + \nabla f \cdot \frac{\boldsymbol{p}}{m}dt + \nabla_p f \cdot \boldsymbol{F}dt \tag{2.10}$$

Dividing the above equation by dt, we obtain the final statement given as,

$$\frac{\partial f}{\partial t} + \nabla f \cdot \frac{\boldsymbol{p}}{m} + \nabla_p f \cdot \boldsymbol{F} = \left(\frac{\partial f}{\partial t}\right)_{coll} \tag{2.11}$$

2.3 Conservation Equations

From the Boltzmann equation, it is possible to obtain the conservation equations identical to the ones described by fluid mechanics by taking n^{th} moments of the equation with the velocity field. The number density is given by,

$$n = \int_{momenta} f d^3\boldsymbol{p} \tag{2.12}$$

and the average value of any function A is given by,

$$\langle A \rangle = \frac{1}{n}\int_{momenta} A f d^3\boldsymbol{p} \tag{2.13}$$

If we multiply the entire Boltzmann equation with A and integrate it with respect to momentum volume, we obtain 4 equations given as,

$$\int A\frac{\partial f}{\partial t}d^3\boldsymbol{p} = \frac{\partial}{\partial t}\left(n\langle A \rangle\right) \tag{2.14}$$

$$\int \frac{p_j A}{m}\frac{\partial f}{\partial x_j}d^3\boldsymbol{p} = \frac{1}{m}\frac{\partial}{\partial x_j}\left(n\left\langle Ap_j \right\rangle\right) \tag{2.15}$$

$$\int AF_j\frac{\partial f}{\partial p_j}d^3\boldsymbol{p} = -nF_j\left\langle \frac{\partial A}{\partial p_j} \right\rangle \tag{2.16}$$

$$\int A \left(\frac{\partial f}{\partial t} \right)_{coll} d^3\boldsymbol{p} = 0 \tag{2.17}$$

If we take the zeroth moment of these equations *i.e.,* $A = m(v_i)^0 = m$ we obtain the conservation of mass equation.

If we take the first moment of these equations *i.e.,* $A = m(v_i)^1 = mv_i$ we obtain the conservation of momentum equation.

If we take the second moment of these equations *i.e.,* $A = m(v_i)^2 = mv_i^2$ we obtain the conservation of energy equation.

2.4 Limitations of the Boltzmann Equation

The primary limitation of the Boltzmann equation is that it assumes that particles are point-sized *i.e.,* they have 0 size. A modification of the Boltzmann equation exists, called the **Enskog equation** and this takes into account the finite size of the particles. Furthermore, no degrees of freedom apart from translation is assumed for particles by the Boltzmann equation. Additionally, many fluids have not only binary but also ternary and higher-order collisions that the Boltzmann equation simply doesn't capture.

CHAPTER 3

Direct Simulation Monte Carlo (DSMC) Method

The DSMC method was first proposed by Graeme Bird [1]. This method is particularly useful for flows where the Knudsen number is past the continuum regime. This method is widely used in Micro Electro Mechanical Systems (MEMS) and the Space Shuttle's re-entry aerodynamics.

DMSC models fluid flows using probabilistic simulation molecules to solve the Boltzmann equation. Being a probabilistic algorithm that considers a set of particles rather than a single particle, it is much more computationally efficient in comparison to Molecular Dynamics. However, this very property of DSMC also makes it susceptible to statistical fluctuation in the solutions.

3.1 The Algorithm

Like any other system consisting of particles, the state of the system is given by the positions and velocities of the particles $\{\boldsymbol{r_i}, \boldsymbol{v_i}\}$ where $i = 1, 2, 3, \cdots, N$ where N is the number of simulated particles in the flow. Each simulated particle corresponds to F_N physical particles with approximately the same positions and velocities. In other words, the volume V of the system is given by,

$$V = \frac{F_N N}{n} \tag{3.1}$$

where n is the number density of the flow.

The evolution of the system is obtained by integrating several properties in time steps τ usually lesser than the mean collision time t_o. This choice is not arbitrary. It is made with the intention of capturing all the physical phenomena with reasonable accuracy. In the absence of external force fields, the particles move ballistically,

$$\boldsymbol{r}_i(t+\tau) = \boldsymbol{r}_i(t) + \boldsymbol{v}_i(t) \cdot \tau \tag{3.2}$$

If and when a particle reaches a particular boundary, its position and velocity are reset according to the boundary condition applied. Once all the particles have been moved according to their velocities and positions, they are put into cells within which they randomly collide with each other based on the collision rates obtained from the *Kinetic Theory of Gases*. After colliding, the velocities of the particles are reset. Statistical sampling is performed and the process is repeated. The entire process is represented in Figure 3.1.

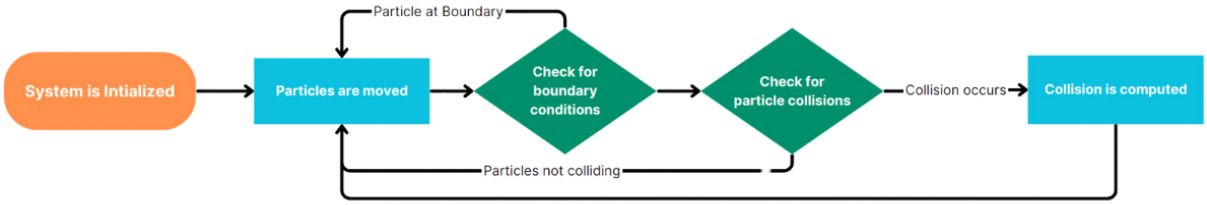

Fig. 3.1: Flowchart explaining a simple DSMC Algorithm

3.2 Collisions

Typically, when we select the dimensions of the collision grid cells, they must be no larger than the mean free path λ. This is to ensure that we get accurate collision statistics in every time step. In methods like Molecular Dynamics, two particles are not considered for a collision if their trajectories are not going to intersect. In DSMC however, all particles within a grid cell are collision candidates regardless of their actual trajectories.

There are several models that describe the collision between any two particles. The **hard spheres model**, for instance, gives the collision probability for a pair of particles i and j as proportional to their relative speed as,

$$P_{coll}[i,j] = \frac{|\boldsymbol{v}_i - \boldsymbol{v}_j|}{\Sigma_{m=1}^{N_c}\Sigma_{n=1}^{m-1}|\boldsymbol{v}_m - \boldsymbol{v}_n|} \tag{3.3}$$

where N_c is the number of particles in the cell.

The double summation in the denominator can be computationally intensive, so DSMC uses a technique called *rejection sampling* to select collision pairs. The steps for rejection sampling are highlighted below : -

1. A pair of candidates particles i, j is chosen at random, and their relative velocity magnitude is computed
2. The pair is accepted as a collision pair if $v_r > v_{r_{max}} \times \mathscr{R}$ where $\mathscr{R}$ is a uniform random number in $[0,1)$.
3. If the pair of particles are accepted, their velocities are reset but their positions are unchanged.

After a collision pair is chosen, the post-collision velocities v_i^* and v_j^* are evaluated. The relative velocity is often conveniently expressed in terms of the spherical angles θ and ϕ and is given by,

$$\boldsymbol{v}_r^* = v_r\left[(sin\theta cos\phi)\hat{x} + (sin\theta sin\phi)\hat{y} + cos\theta\hat{z}\right] \tag{3.4}$$

and these angles are selected by some Monte Carlo processes with distributions given by the selected collision model. For the hard spheres model, these angles are uniformly distributed over the unit sphere. The azimuthal angle is between 0 and 2π, and is written as $\phi = 2\pi\mathscr{R}_1$ where $\mathscr{R}_1$ is a uniform deviate in $[0,1)$. The polar angle is distributed according to,

$$P_\theta(\theta)d\theta = \frac{1}{2}sin\theta d\theta \tag{3.5}$$

Using the change of variables, $q = -cos\theta$, we obtain,

$$P_q(q)dq = \frac{1}{2}dq \tag{3.6}$$

where we can write $q = 2\mathscr{R}_2 - 1$ where $\mathscr{R}_2$ is a uniform deviate in $[0,1)$.

The post-collision velocities are set as given by the equation below,

$$\boldsymbol{v}_i^* = \boldsymbol{v}_{cm}^* + \frac{1}{2}\boldsymbol{v}_r^* \qquad \boldsymbol{v}_j^* = \boldsymbol{v}_{cm}^* - \frac{1}{2}\boldsymbol{v}_r^* \tag{3.7}$$

As we expect from the conservation of linear momentum and energy, the velocity of the centre of mass and the relative speed between the particles doesn't change. This process of computing collisions is repeated for every pair of particles. The total number of hard sphere collisions in a given cell during a timestep τ is given by,

$$M_{coll} = \frac{1}{2}(N_c - 1)F_N f_{coll}\tau = \frac{N_c(N_c-1)F_N\pi d^2\langle v_r\rangle\tau}{2V_c} \tag{3.8}$$

where f_{coll} is the collision frequency given by the Kinetic Theory of Gases, d is the diameter of the cell and V_c is the volume of the cell. The ratio of the total accepted to the total number of candidates for hard sphere particles are given by,

$$\frac{M_{coll}}{M_{cand}} = \frac{\langle v_r\rangle}{v_r^{max}} \tag{3.9}$$

CHAPTER 4

SPARTA

SPARTA is an acronym for Stochastic PArallel Rarefied-gas Time-accurate Analyzer. SPARTA was developed by Sandia National Laboratories under the US Department of Energy. The chief authors of SPARTA are Michael Gallis, Steve Plimpton, and Stan Moore. Plimpton et al. (2019) describe how SPARTA functions in their work on implementing DSMC on petaflop supercomputers [4].

SPARTA is a parallel DSMC code for performing simulations of low-density gases in 2D or 3D. Particles advect through a hierarchical Cartesian grid that overlays the simulation box. The grid is used to group particles by grid cell for purposes of performing collisions and chemistry. Physical objects with triangulated surfaces can be embedded in the grid, creating cut and split grid cells. The grid is also used to efficiently find particle/surface collisions. Since the fundamental DSMC algorithm is inherently parallel, the challenge is not to parallelize the code but to balance computations across a large number of processors.

SPARTA has three kinds of data : particles, grid cells, and optionally surface elements. The grid used by SPARTA is a rectilinear hierarchical grid *i.e.,* each grid cell can have more grid cells within itself, recursively. All these child grid cells are also cuboidal in shape. Figure 4.1 was taken from [4] and represents the hierarchical grid around the Apollo space capsule.

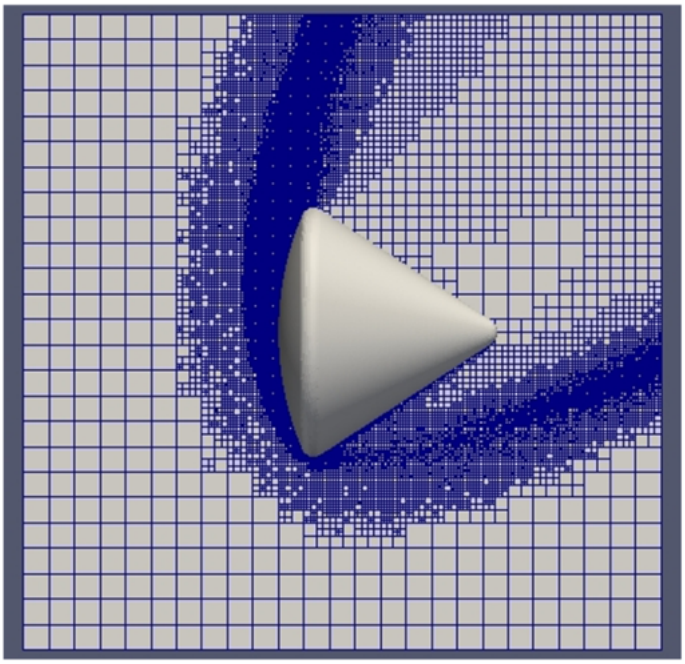

Fig. 4.1: A 2D slice of a 3D hierarchical grid around the Apollo space capsule [Source : [4]]

SPARTA has the ability to run parallely by assigning certain grid cells to certain processors. An example is given in Figure 4.2 which was taken from [4] where each color represents a particular processor.

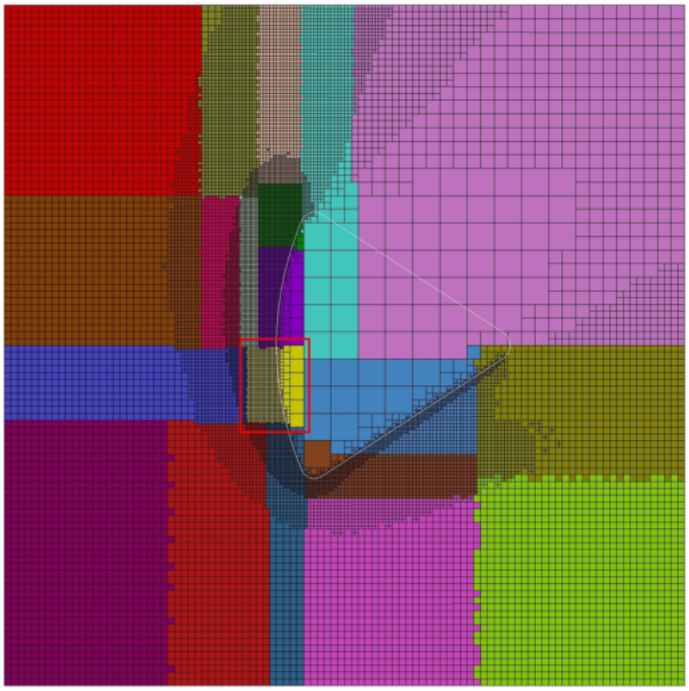

Fig. 4.2: A 5-level 2D hierarchical grid around the Apollo space capsule [Source : [4]]

There have been several bench-marking problems to show that SPARTA indeed does provide

physically accurate solutions and some of them will be discussed subsequently.

4.1 Effect of Slip on Vortex Shedding

This study was done by Gallis and Torczynski [2] to analyse the effect of slip on the vortex shedding in a flow around a circular cylinder. Typically most studies assume that the no-slip condition applies on the cylinder surface. They perform their simulations at a Reynolds number of 100, a Mach number of 0.3 and a corresponding Knudsen number of 0.0048. The simulation domain is described in Figure 4.3 taken from [2].

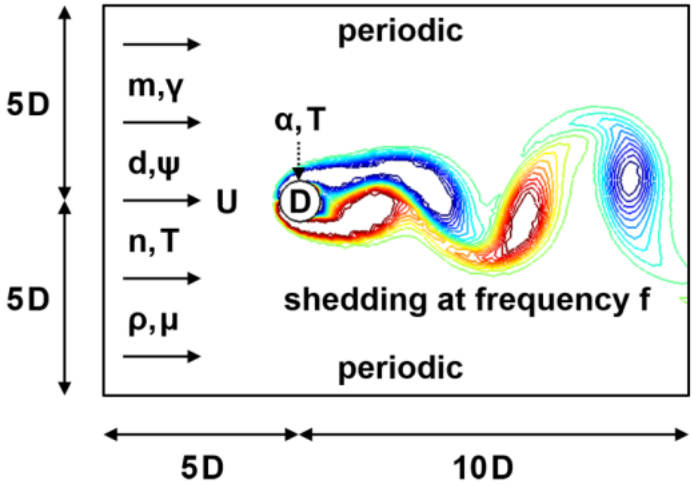

Fig. 4.3: Simulation domain [Source : [2]]

The cylinder diameter D was chosen to be 1 m for convenience. The gas was assumed to be Argon-like with a molecular mass of $m = 66.3 \times 10^{-27} kg$, specfic heat ratio $\gamma = 5/3$, viscosity $\mu = 2.117 \times 10^{-5} Pa\,s$ at temperature $T = 273.15K$. For the non-dimensional numbers described above, the freestream velocity, density, number density and molecular mean free path are $U = 92.37 m/s$, $\rho = 2.292 \times 10^{-5} kg/m^3$, $n = 3.457 \times 10^{20} 1/m^3$ and $\lambda = 0.0048m$. The grid cell size is chosen to be about one-fourth the mean free path and the time step is chosen to be about one-fourth of the mean collision time. There are about 100 particles per grid cell, totaling about 8 billion particles. The cylinder's surface reflects diffusively with a probability α and specularly with a probability $1 - \alpha$ where α is the **accommodation coefficient**.

The same simulation was also performed using CFD on COMSOL Multiphysics and the results were compared. Figure **??** was taken from their work [**gallus2021effect**] and highlights that the

results are largely in agreement with each other, with DSMC being a little bit more noisy than CFD due to its statistical nature.

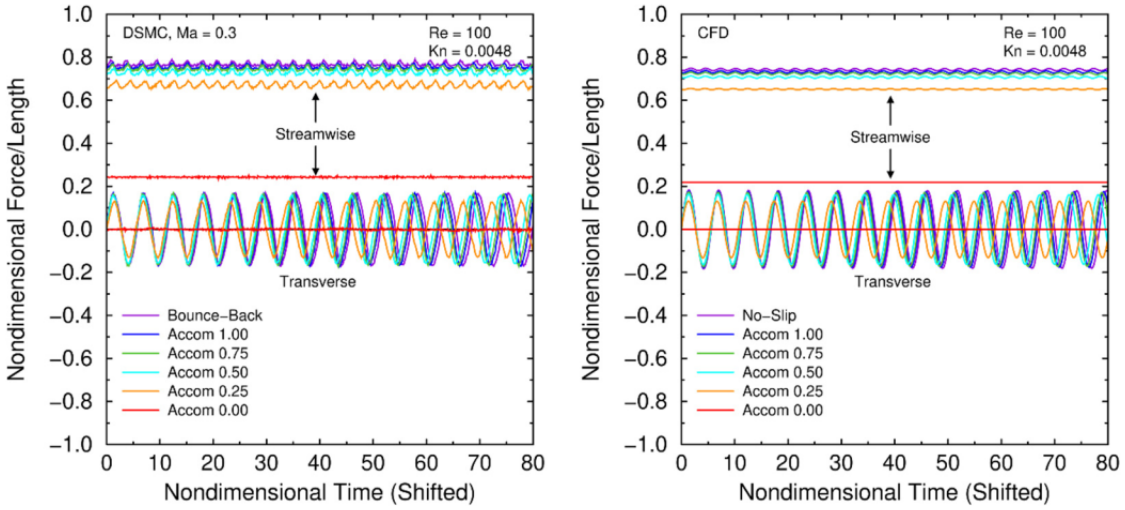

Fig. 4.4: DMSC (left) and CFD (right) force histories at late times with periodic vortex shedding [Source : [2]]

Clearly, the CFD and DSMC simulations are in good agreement, indicating that the DSMC method is physically accurate. However, for low Mach number (and consequently low Knudsen numbers), CFD is a lot more computationally efficient as simulating particle collisions under these conditions is extreme. Almost all the physical phenomena can be captured by conventional mathematical models like the Navier-Stokes equations.

In the upcoming chapters, some of my own simulations using SPARTA and their results will be discussed.

CHAPTER 5

1D Fourier Flow

The one-dimensional heat equation is one of the simplest partial differential equations and can be solved analytically. It is given by,

$$\frac{\partial u}{\partial t} = \frac{\partial^2 u}{\partial x^2} \tag{5.1}$$

where u is the temperature field. The steady-state solution will always be a linear function between the two boundary temperatures. Simulations have been performed using SPARTA to obtain the solution to this heat equation for higher Knudsen numbers.

5.1 Setup

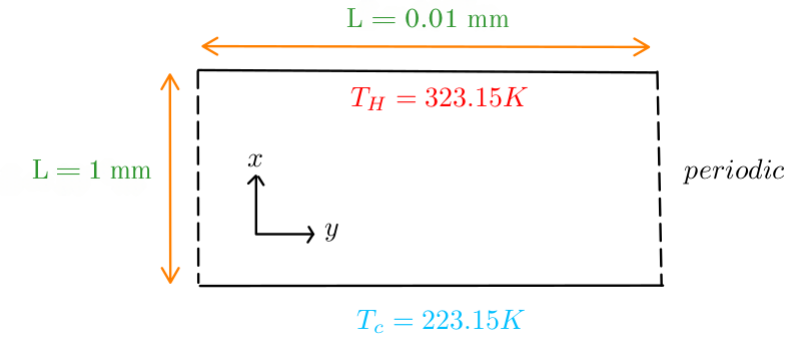

Fig. 5.1: Setup of the simulation

For all the simulations, the gas is chosen to be Argon, with a molecular mass of $m = 6.63 \times 10^{-26} kg$ and a diameter of $d = 3.658 \times 10^{-10} m$. The simulation domain is chosen as given in Figure 5.1. Since SPARTA doesn't have support for 1D simulations, the choice of the domain is made such that the x-direction is much larger than the y-direction, to approximate the domain as 1 dimensional.

At the mean temperature between T_C and T_H, the most probable speed of the molecules is obtained using the expression given below,

$$v_{mps} = \sqrt{\frac{2k_B T}{M}} \tag{5.2}$$

where $k_B = 1.38 \times 10^{-23} J/K$ is the Boltzmann constant, T is the temperature of the particle and M is the molecular mass of the particle. Substituting for these values, we get the most probable speed for Argon under the conditions of the simulation is $v_{mps} \approx 337.208 m/s$. The mean free path for a monoatomic molecule is given by,

$$\lambda = \frac{1}{\sqrt{2}\pi n d^2} \tag{5.3}$$

where n is the number density of the particle in the domain and d is the molecular diameter of the particle. Substituting the value of d in the expression, we obtain,

$$\lambda \approx \frac{1.682 \times 10^{18}}{n} \tag{5.4}$$

Using the expression for the Knudsen number given in Equation 1.2, we obtain,

$$Kn = \frac{1.682 \times 10^{21}}{n} \tag{5.5}$$

where $10^{-3} m$ is taken to be the characteristic length scale of the problem. To obatin a Knudsen number of 0.1, which is in the transitional regime, we must have $n = 1.682 \times 10^{22} kg/m^3$. Once the number density is known, we can find the number of particles in the domain N using,

$$N = nV \tag{5.6}$$

where V is the volume of the simulation domain. Since SPARTA takes the z-dimension to be 1 for 2D simulations, we obtain the volume as,

$$V = \Delta x \Delta y \Delta z = \left(10^{-3} \times 10^{-8} \times 1\right) m^3 = 10^{-8} m^3 \tag{5.7}$$

Consequently, the number of particles in the domain is calculated to be $N = 1.682 \times 10^{14}$. Similarly, the mean collision time can be calculated using,

$$t_o = \frac{\lambda}{v_{mps}} \tag{5.8}$$

and this evaluates to $t_o \approx 2.966 \times 10^{-7} s$. We pick the grid cell size and time step size to keep them smaller than λ and t_o respectively, and will use $\tau = 10^{-8} s$ as the timestep and $(100 \times 1 \times 1)$ grid cells in the domain.

Now that the number of grid cells is fixed, we can calculate the number of simulated particles by picking the number of particles that each grid cell contains. Depending on the number of particles we pick, the simulations will be slightly different. I have selected two such numbers, 20 particles per grid cell and 100 particles per grid cell to see how the number of simulated particles affects the solution.

5.2 Solution for 20 Particles per Grid Cell

If we choose to have 20 particles per grid cell, and 100 grid cells in total, that implies that we have to use 2000 simulated particles in the simulation. Since the total number of particles is fixed, the simulation ratio can be found as $F_N = 8.41 \times 10^{10}$. The simulation is run for a million steps yielding a total physical time of 0.01 seconds. The parameter for convergence is chosen to be the global temperature. Plots of some representative time steps are highlighted below. All the plots and the video files showing the evolution of the system can be found in the repository

containing the project [6].

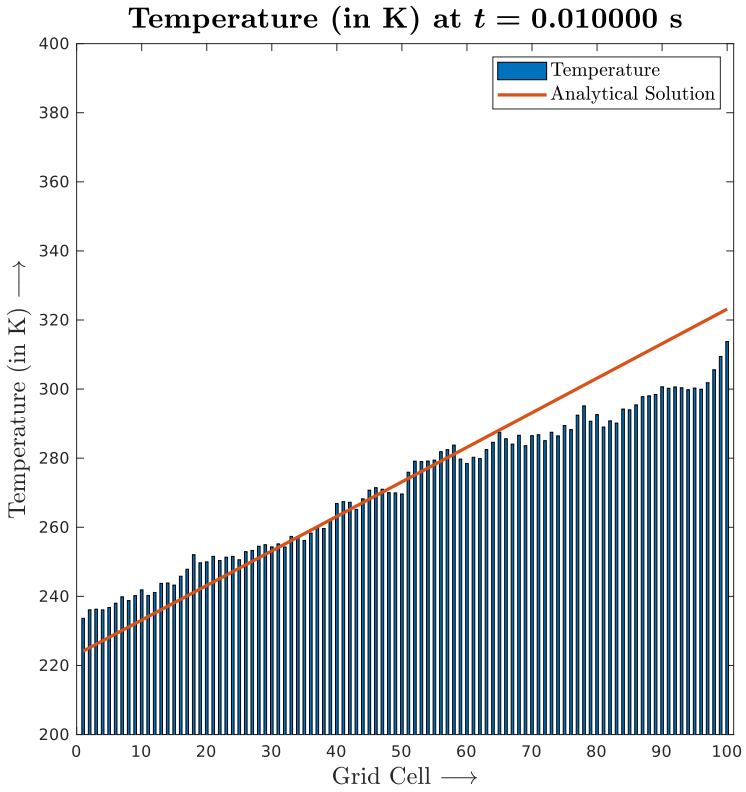

Fig. 5.2: Solution obtained through SPARTA for 20 particles per grid cell

We can clearly see that the temperature profile obtained through DSMC appears roughly linear, but the slope doesn't match the slope that is expected from the analytical solution. One can also see that the fluctuations in the solution are evident with there being random spikes in the solution. The reason for the slope not matching will be described in detail in the next few pages.

5.3 Solution for 100 Particles per Grid Cell

If we choose to have 100 particles per grid cell, and 100 grid cells in total, that implies that we have to use 10000 simulated particles in the simulation. Since the total number of particles is fixed, the simulation ratio can be found as $F_N = 1.682 \times 10^{10}$. The simulation is run for a million steps yielding a total physical time of 0.01 seconds. The parameter for convergence is chosen to be the global temperature. Plots of some representative time steps are highlighted below. All the plots and the video files showing the evolution of the system can be found in the repository

containing the project [6].

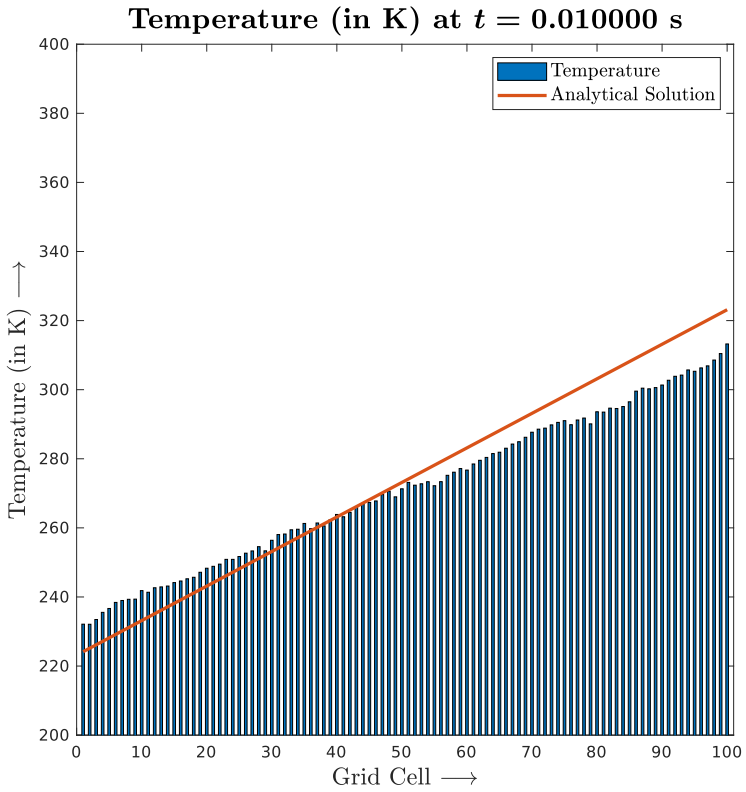

Fig. 5.3: Solution obtained through SPARTA for 100 particles per grid cell

We can clearly see that the temperature profile obtained through DSMC appears roughly linear, but once again, the slope doesn't match the slope that is expected from the analytical solution. One can also see that the fluctuations in this solution are much lesser than that in Figure 5.2. This is as expected. When we increase the number of simulated particles, the statistical fluctuations in the solution start to reduce.

5.4 Deviation of the Solution from the Analytical Slope

From Figures 5.2 and 5.3, it is evident that at the temperature plates, the temperatures are different from what is actually applied. As a result, the slope of the solution also changes. The claim is that this is an effect due to the higher Knudsen number of the flow. To prove this conclusively, let's consider the following adjustments to the problem.

5.4.1 Case 1 : Resolving the Grid

Just to verify that the mismatching slopes is not due to the grid not being resolved sufficiently, let's resolve the grid to $(200 \times 1 \times 1)$ and see what happens to the solution. Considering the same 100 particles per grid cell to reduce fluctutations, the number of simulated particles will now become 20000. To keep the total number of physical particles the same, the simulation ratio F_N will become 8.41×10^9. The plot of the temperature profile at the same instant but for 200 grid cells is given in Figure 5.4.

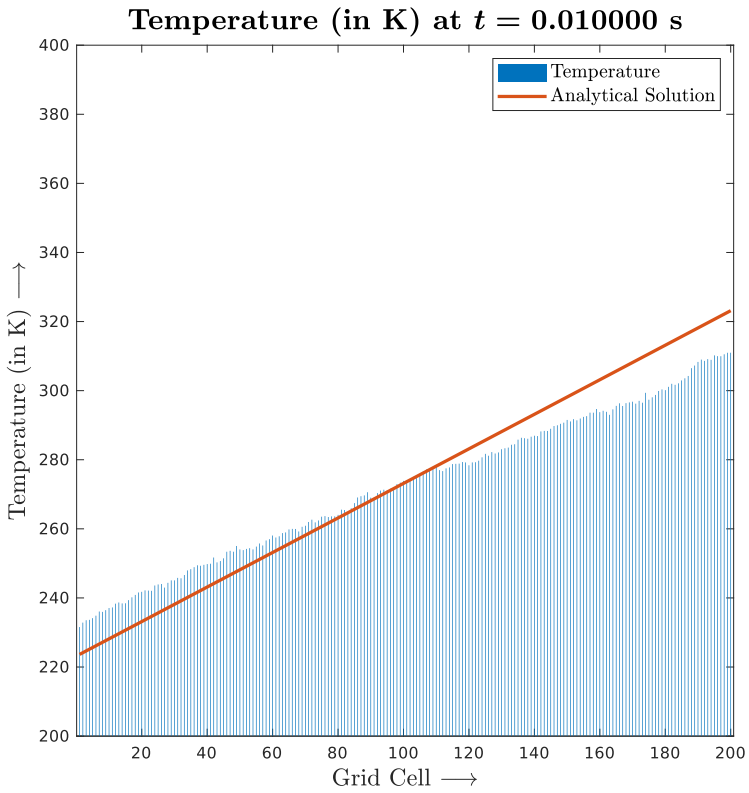

Fig. 5.4: Solution obtained through SPARTA for 200 grid cells

Notice how the solution in Figure 5.4 resembles the solution in Figure 5.3 almost identically. This allows us to conclude safely that the disparity in the slope is not due to the resolution of the grid.

5.4.2 Case 2 : Changing the Knudsen Number

Now to see that the disparity in the slopes is indeed an effect of rarefraction of the flow, we shall perform the simulation for a flow with a Knudsen number of 0.02. Since the knudsen number is decreased by a factor of 5, the number of particles must increase by a factor of 5. For 100 grid cells, and the same 100 particles per grid cell, the number of simulated particles is 10000. But to obtain the new Knudsen number of 0.02, the simulation ratio must be set to $F_N = 8.41 \times 10^{10}$. If we plot the solution at the same time step as the above solutions, we obtain Figure 5.5.

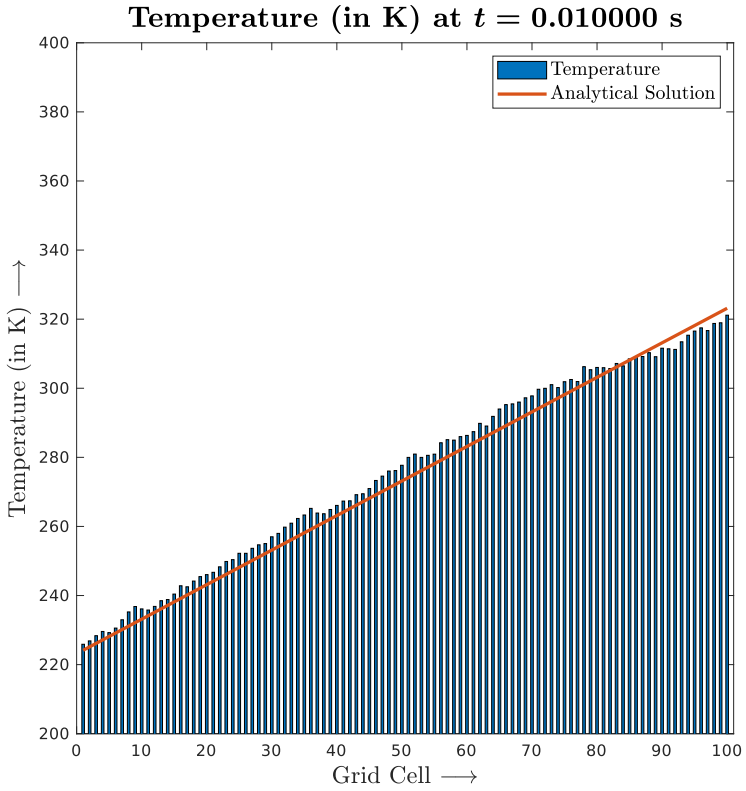

Fig. 5.5: Solution obtained through SPARTA for $Kn = 0.02$

Clearly, in Figure 5.5, the solution is a much closer match to the theoretical slope. This further strengthens the argument that the disparity in the slopes is a rarefraction effect that vanishes with decreasing the Knudsen number. In fact, this phenomenon is well known and the region around the boundary in which these deviations occur is called **knudsen layers**. Rader et al. (2005) also describe the effect of these Knudsen layers [5].

CHAPTER 6

2D Flow Around a Cylinder

SPARTA has built-in support for 2D simulations. Additionally, it also has the ability to render particles and surfaces in the simulation through ray tracing at any instant of time. These features have been utilized and are discussed in this chapter.

6.1 Setup

The setup for the simulation is represented in Figure 6.1.

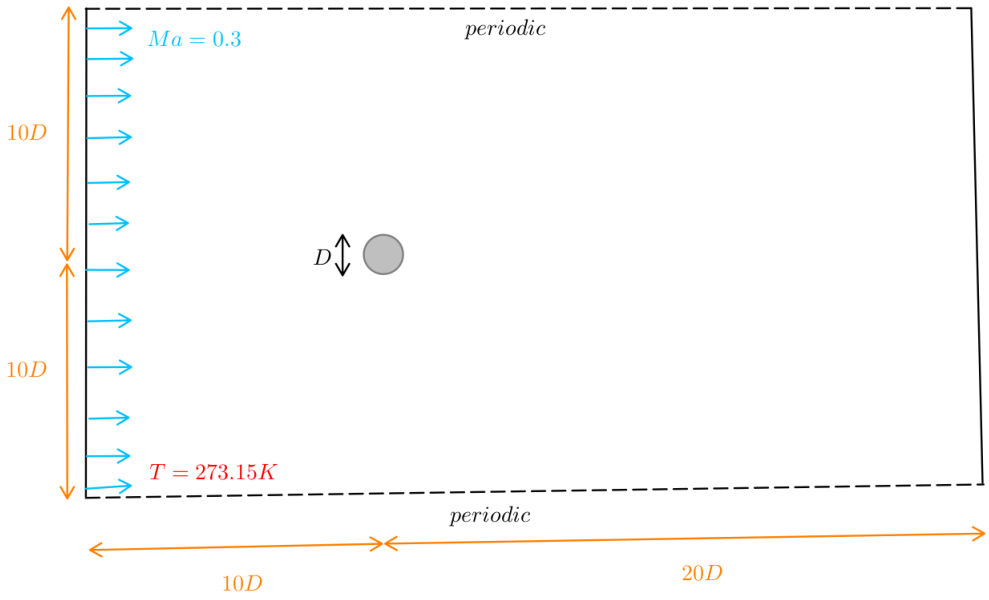

Fig. 6.1: Setup of the simulation

There is a circular cylinder of diameter $D = 0.01m$ placed in the flow and the domain selected to be large in comparison to the cylinder to reduce boundary effects in the simulation. The extent of the domain behind the cylinder is longer than the domain ahead as the wake that is formed behind a cylinder is often quite complex and is of more interest in general. The flow at the inlet is set to be at a uniform $Ma = 0.3$ where compressibility effects just start to appear and the temperature is kept at 273.15 K throughout the inlet.

The hierarchical grid that SPARTA provides is utilised in this simulation, where there $(30 \times 20 \times 1)$ grid cells in the first level called the *sampling cells*. These sampling cells are used to sample the macroscopic properties such as temperature and pressure throughout the domain. However, these cells are too large for there to be accurate collision statistics within them, so each sampling cell is further divided into $(2 \times 2 \times 1)$ *collision cells*. Each of these collision cells has about 62.5 particles in them. The simulation ratio F_N is taken to be 6.72×10^{14} and this yields $N = 1.01 \times 10^{20}$. If we account for the volume of the simulation domain and use Equation 5.3 to calculate the mean free path as $\lambda = 0.001$ when we consider the gas to be Argon. Using Equation 1.2, we can calculate the Knudsen number of the simulation to be about 0.1. Since the Knudsen number and the Mach number of the flow are known, the Reynolds number can be found using,

$$Kn = \frac{Ma}{Re}\sqrt{\frac{\gamma\pi}{2}} \tag{6.1}$$

From the above equation, we obtain $Re \approx 4.59$. We also obtain the mean collision time from Equation 5.8 as $t_o \approx= 3 \times 10^{-6}s$ and hence the time step is chosen to be $\tau = 3 \times 10^{-7}s$ and the simulation is performed for a million timesteps, yielding a total physical time of 0.3 s.

6.2 Ray Traced Images

This section gives some ray-traced images given by SPARTA. These images can be output for any simulation, from any orientation, and serve as a valuable way to visualize the flow. The images for every timestep can be found in [6].

Figure 6.2 gives an image of the flow at the $950,000^{th}$ step of the simulation. One can observe that the particles seem to be closer to each other before the cylinder than they are after. We can infer this as the region before the cylinder has a lot more red spots than the region after.

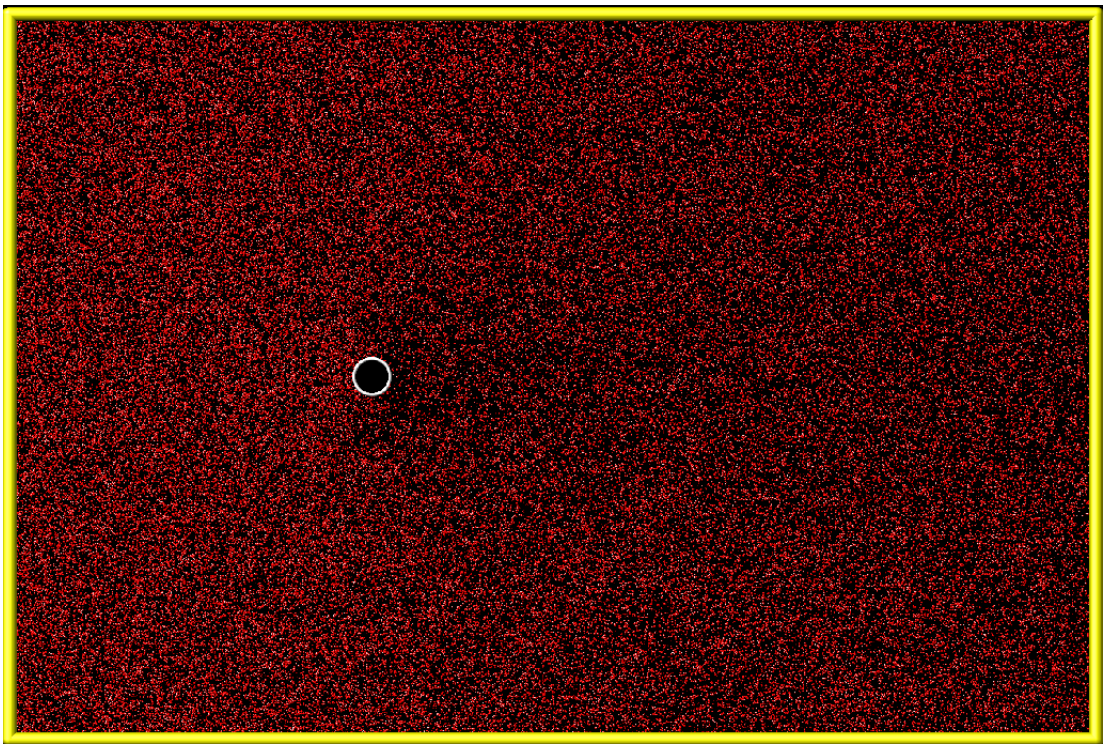

Fig. 6.2: Ray Traced Image of the Flow

It can be seen that the region behind the cylinder has fewer particles than the region in front. This is a very crude representation of the wake that is formed behind the cylinder under these flow conditions.

Apart from these observations, since the flow at the inlet is uniform and the cylinder is placed symmetrically about the vertical extents of the domain, we can expect the flow to be symmetric. If the flow is symmetric, then we expect the lift to be zero around the cylinder while the drag is along the positive x-direction. Figures 6.3 and 6.4 show exactly that.

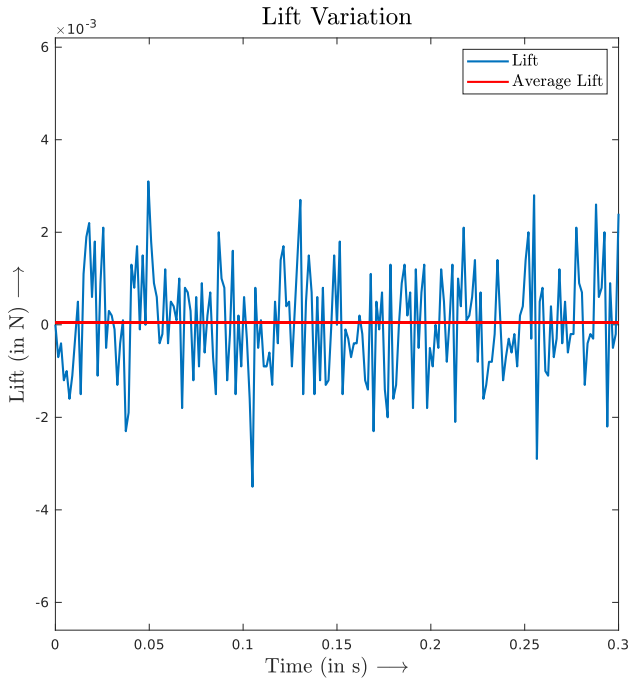

Fig. 6.3: Lift variation with time

Notice how in Figure 6.3 the average lift is nearly 0 while in Figure 6.4, the average drag is orders of magnitude higher and non-zero. One can also see the transience as drag increases from zero to its steady-state value near the beginning of the simulation.

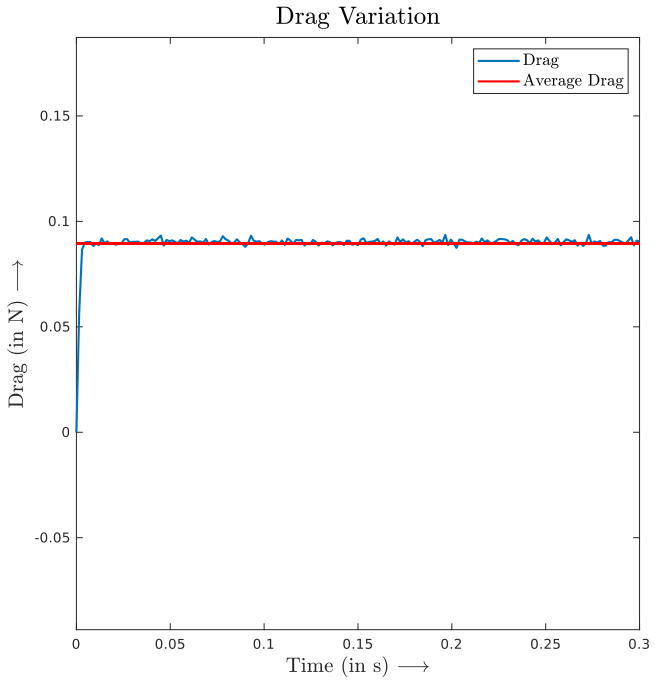

Fig. 6.4: Drag variation with time

CHAPTER 7

Future Directions

So far in this project, the work has primarily revolved around utilizing SPARTA to reproduce results of well-known physical phenomena. So far 1D and 2D phenomena have been reproduced with great accuracy. However, there are several new setups that can be explored. One such change would be to start utilizing **polyatomic molecules** instead of the monoatomic Argon that has been used so far. This is one of the true strengths of SPARTA as it's very difficult to obtain analytical solutions for such flow problems when considering polyatomic molecules due to the higher degrees of freedom available. Furthermore, 3D simulations can be performed, visualized, and compared with experimental data and can even be used to explain experimentally obtained results.

One idea that is interesting is to simulate the flow around a sphere in Martian conditions. This problem is particularly fascinating as it not only involves conditions where experiments are harder to be performed, but it also falls right in the strength of SPARTA as the atmosphere in Mars is far more rarefied than the atmosphere on Earth. The most abundant gas in the Martian atmosphere is carbon dioxide which is polyatomic. The temperatures and pressures vary quite a lot on Mars. Lastly, there is also a growing interest in space expeditions to Mars, and such studies on the Martian atmosphere are filled with potential breakthroughs in our understanding of interplanetary expeditions. All these characteristic features of the Martian atmosphere problem put together make this a particularly interesting and promising area of research. Some data pertaining to the Martian atmosphere has been presented in the following section.

7.1 Martian Atmosphere

Mars has a very unique atmosphere. Unlike Earth's warm atmosphere, the temperatures on Mars lie predominantly between 166 K and 256 K, which is well below the freezing point of water at sea level. The atmosphere at Mars is also very thin, having a mean atmospheric pressure of about 600 Pa in comparison to Earth's 110,000 Pa. One feature that can be observed nowhere on Earth is the low thermal inertia that the Martian atmosphere possesses. Temperature swings of the order of 100 K can happen over short durations of time. There are also *katabatic* winds on Mars, which are winds that are accelerated down a slope by gravity and a density gradient. These are similar to the katabatic winds found in some places like Greenland. Another feature that leads to some very interesting phenomena is the presence of atmospheric electricity on Mars. Some of these phenomena have been described by Rahman *et al.* [7].

7.1.1 Descent Characteristics

Over here, the pressure, temperature, and density of the Martian atmosphere are described using the data obtained by NASA's Curiosity Rover from the Planetary Data System [3]. Figure 7.1 shows the variation of atmospheric temperature with height.

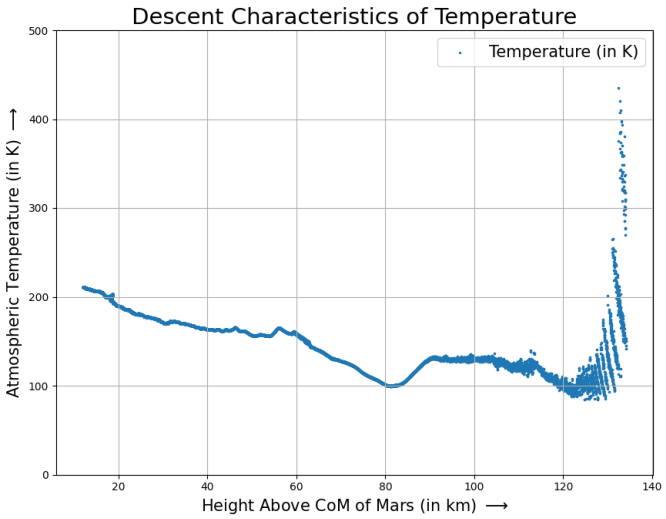

Fig. 7.1: Variation of atmospheric temperature with height on Mars

One can see that the temperature is high at the upper layers of the atmosphere, obtains a minima

somewhere in between and again increases towards the surface of the planet. This can be attributed to a combination of solar radiation, the thermal radiation of the surface of Mars and, the low thermal conductivity of air. This variation is qualitatively similar to the variation on Earth, represented in Figure 7.2.

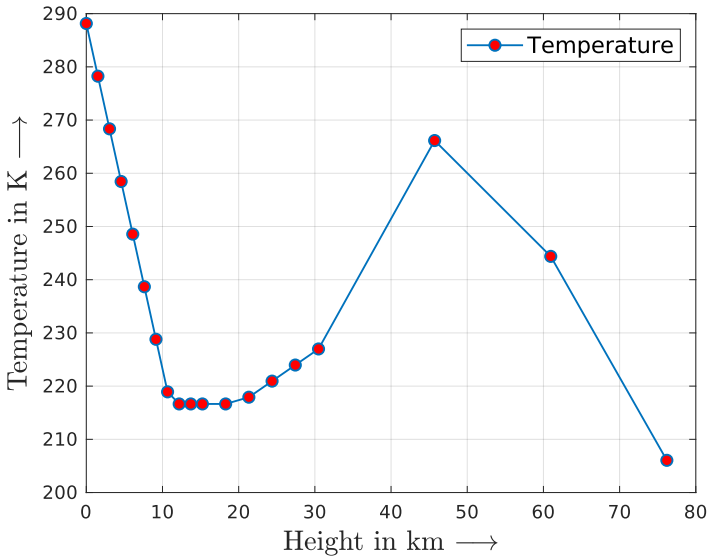

Fig. 7.2: Variation of atmospheric temperature with height on Earth

Figure 7.3 shows the variation of atmospheric pressure with height. Notice how this decreasing linear profile on a logarithmic scale suggests an exponential decay in pressure, much like what is observed on Earth (Figure 7.4).

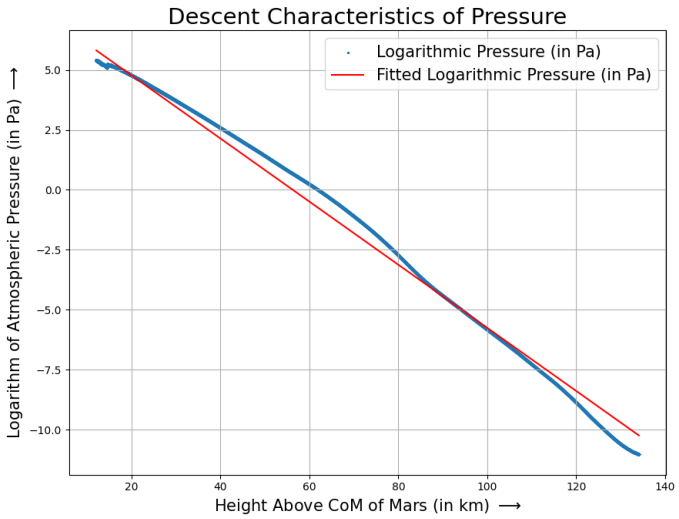

Fig. 7.3: Variation of atmospheric pressure with height on Mars

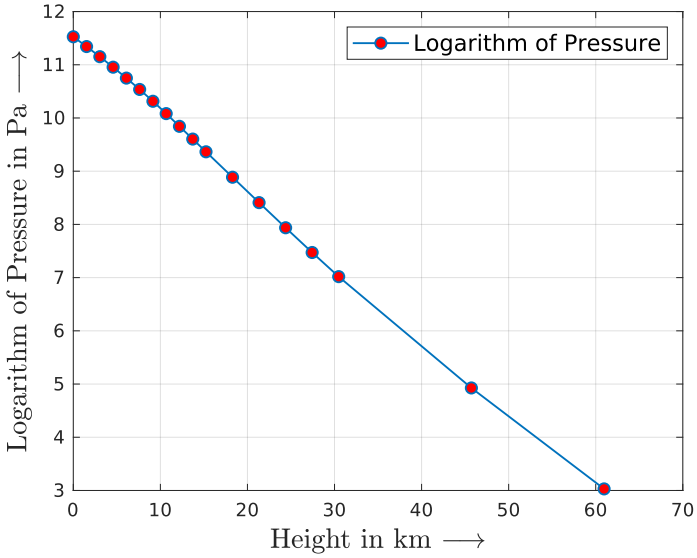

Fig. 7.4: Variation of atmospheric pressure with height on Earth

Figure 7.5 shows the variation of atmospheric density with height. Notice how this decreasing linear profile on a logarithmic scale suggests an exponential decay in density, much like what is observed on Earth (Figure 7.6). This close qualitative matching of the properties of Earth and the Martian atmosphere is very interesting, implying only a scale difference between the two planets on a high level.

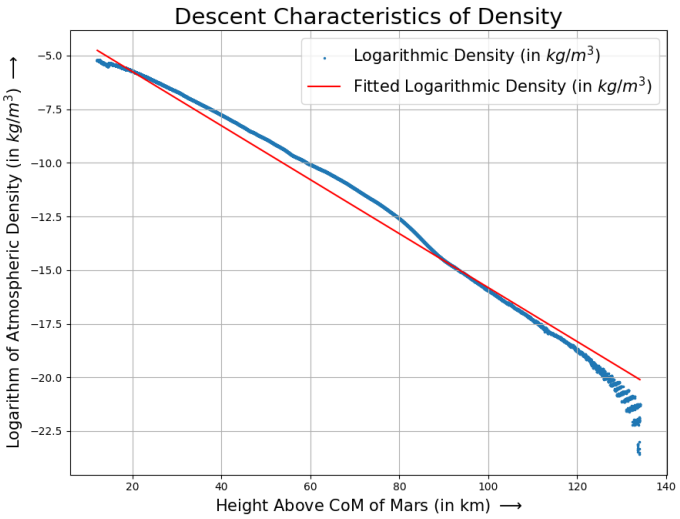

Fig. 7.5: Variation of atmospheric density with height on Mars

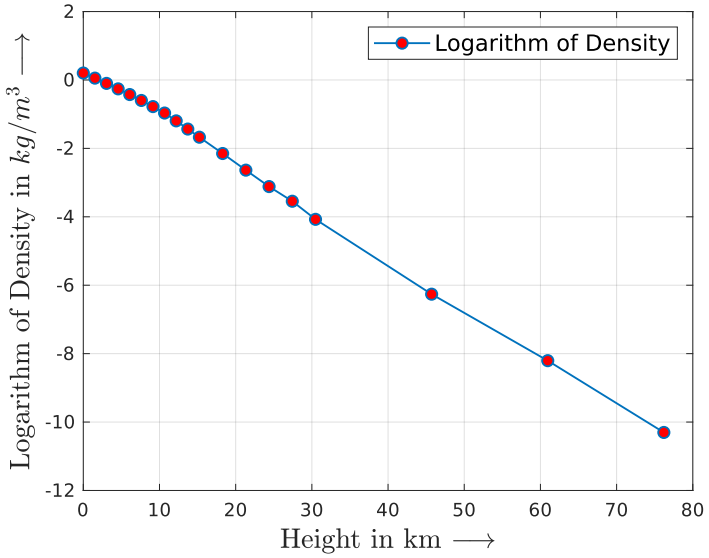

Fig. 7.6: Variation of atmospheric density with height on Earth

7.1.2 Chemical Composition

The chemical composition of Mars is quite different from that observed on Earth. Below, the data from a few experiments from the Mars Science Laboratory's Reduced Data Records (RDR) repository [8] are plotted. Again, all of the plots, the code to scrape the data from RDR, and the plots are available in the repository containing this project [6].

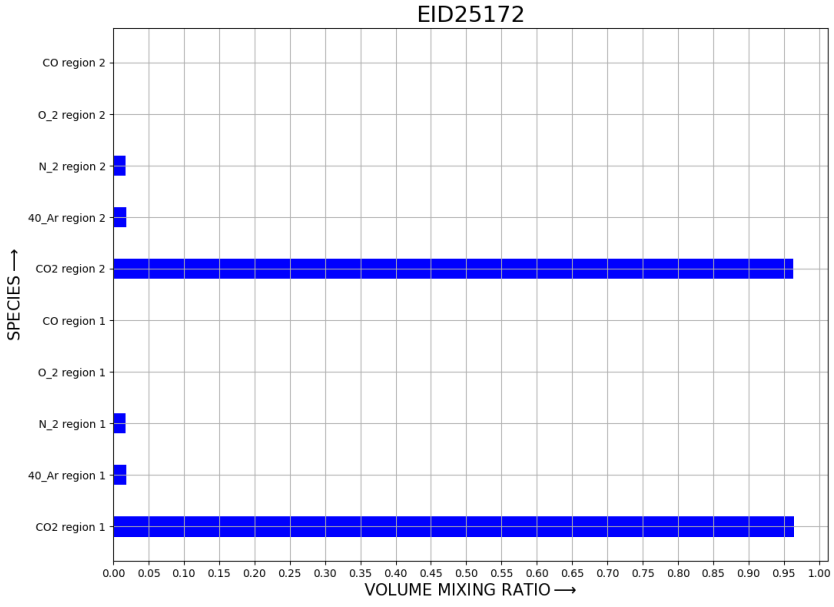

Fig. 7.7: Relative abundance of compounds in the Martian atmophere

The final data presented are the **volume mixing ratios** of various compounds in the Martian atmosphere obtained using the **Quadrupole Mass Spectrometer** (QMS) present on the Curiosity rover. Figure 7.7 gives a representative plot of the data in RDR. From the plot, we can clearly infer that carbon dioxide is the most prominent gas in the Martian atmosphere, followed by nitrogen and argon.

CHAPTER 8

Conclusions

We started by understanding the underlying assumptions of continuum fluid mechanics, and the conditions under which these assumptions start to fail. Progressing from there, we looked at alternative methods to model fluid flow in these regimes where continuum assumptions fail, exploring the mathematical tools on a broad level. After gaining a preliminary understanding of the underlying mathematics and physics, we discuss the Direct Simulation Monte Carlo (DSMC) algorithm to simulate such flows. Consequently, we moved on to introduce an open-source tool called SPARTA and explored some existing studies that verify its validity by comparing it with accepted findings.

We then moved on to utilizing SPARTA for our simulations, starting with 1D Fourier Flow where we solved the system for 1D heat transfer under various conditions, exploring deviations and providing the reasons for the same. After, this we moved on to 2D simulations of flow around a cylinder and explored ray tracing tools to visualize the flow. We also plotted the lift and drag variations to see if we indeed got the lift and drag values that we expected.

In the end, we discussed some future directions that one can explore with SPARTA and pointed out an interesting problem involving the Martian atmosphere. Some relevant data and their visualizations were also provided and discussed.

Bibliography

[1] Graeme A Bird. *Molecular gas dynamics and the direct simulation of gas flows*. Oxford university press, 1994.

[2] Michail A Gallis and John R Torczynski. "Effect of slip on vortex shedding from a circular cylinder in a gas flow". In: *Physical Review Fluids* 6.6 (2021), p. 063402.

[3] C Holstein-Rathlou, A Maue, and P Withers. "Atmospheric studies from the Mars Science Laboratory Entry, Descent and Landing atmospheric structure reconstruction". In: *Planetary and Space Science* 120 (2016), pp. 15–23.

[4] Steve J Plimpton et al. "Direct simulation Monte Carlo on petaflop supercomputers and beyond". In: *Physics of Fluids* 31.8 (2019).

[5] Daniel Rader et al. "DSMC Convergence Behavior for Fourier Flow". In: *AIP Conference Proceedings* 762 (May 2005), pp. 473–478. DOI: 10.1063/1.1941581.

[6] Pradyumnan Raghuveeran. *Work During Summer Research Fellowship Programme 2024 Under Prof. Meheboob Alam*. May 2024. URL: https://github.com/Prad-R/SRFP_2024_Project.git.

[7] Mustafa Mutiur Rahman, Ahmed Saieed, and Jean-Pierre Hickey. "Turbulence-induced electrical discharges in charged particle-laden Martian boundary layers". In: *Flow* 3 (2023), E34.

[8] SAM Reduced Data Record RDR. "Mars Science Laboratory (MSL) Software Interface Specification". In: (2013).